

RESEARCH ARTICLE

[View Article Online](#)
[View Journal](#) | [View Issue](#)



Cite this: *Inorg. Chem. Front.*, 2025,
12, 8110

Construction of carbon nanotube-supported CuO–Fe₃O₄ dual-site catalysts for ambient electrosynthesis of ammonia

Shun Zhang,^{a,b} Shengbo Zhang,^{ID *}^{a,b} Jiafang Liu,^{ID}^{a,b} Zhixian Mao,^{a,b} Yunxia Zhang,^{ID}^{a,b} Guozhong Wang,^{ID}^{a,b} Huajie Yin,^{ID}^{a,b} and Haimin Zhang ^{ID *}^{a,b}

The electrocatalytic nitrate (NO₃[−]) reduction reaction (NitRR) to ammonia (NH₃) is considered a sustainable and environmentally friendly approach for synthesizing ammonia. However, the electrocatalyst encounters challenges related to the limited distribution of NO₃[−] and insufficient active hydrogen on the catalyst surface, which result from the high concentration of NO₃[−] and the difficulty of water splitting under ambient conditions. Here, by introducing Cu and Fe oxides onto carbon nanotube substrates (CuO–Fe₃O₄/CNTs), a CuO–Fe₃O₄ dual-site synergistic catalytic mechanism is proposed to promote the adsorption and conversion of NO₃[−] at Cu species sites and accelerate water splitting at Fe species sites, thereby significantly enhancing the performance of nitrate reduction reactions. The as-synthesized CuO–Fe₃O₄/CNTs exhibits good activity for the NitRR, achieving an NH₃ yield rate of 39.2 ± 3.5 mg h^{−1} mg_{cat}^{−1} and a faradaic efficiency of 90.5 ± 2.2% at −0.8 V (vs. RHE). Furthermore, different *in situ* characterizations were employed to identify intermediates in the electrocatalytic NitRR process, confirming CuO–Fe₃O₄/CNTs as a promising catalyst for NH₃ electrosynthesis.

Received 21st July 2025,
Accepted 29th September 2025

DOI: 10.1039/d5qi01543j

rsc.li/frontiers-inorganic

Ammonia (NH₃) is a crucial chemical in modern society, widely used across various industries.^{1–3} The conventional method for NH₃ synthesis is the Haber–Bosch process, which uses hydrogen obtained from water electrolysis and nitrogen from the air as feedstocks.^{4,5} Although these raw materials are relatively inexpensive, the process is highly energy-intensive and produces significant CO₂ emissions, posing serious environmental concerns.^{6,7} Additionally, the low solubility of N₂ in water and the high dissociation energy of the N≡N bond (941 kJ mol^{−1}) further limit its practical application.^{8,9} In contrast, nitrate (NO₃[−]), with a much lower N=O bond dissociation energy (204 kJ mol^{−1}), is considered a promising alternative nitrogen source due to its abundance.^{10,11} With industrial development, increasing amounts of nitrate-containing wastewater are being released into the environment.¹² Utilizing nitrate as a nitrogen source offers a dual benefit: reducing energy consumption in NH₃ production and mitigating water pollution caused by nitrate.^{13–16} The electrocatalytic nitrate reduction reaction (NitRR) for ammonia synthesis has emerged as a promising new approach in recent years,

enabling both wastewater treatment and continuous ammonia generation.^{17,18} However, the NitRR involves a complex eight-electron transfer process with multiple reaction pathways and intermediates, which hinders the efficient conversion of NO₃[−] to NH₃.¹⁹ Therefore, there is an urgent need for a catalyst that can achieve both high faradaic efficiency and high selectivity for ammonia production.

The electrochemical NitRR to NH₃ is a multi-step cascade process that commences with water activation for the generation of active hydrogen atoms (*H), followed by the sequential hydrogenation of adsorbed NO₃[−] species.²⁰ The competition for active sites on traditional single-active-site electrocatalysts significantly reduces the efficiency and selectivity of NH₃ electrosynthesis from NO₃[−].²¹ In particular, in nitrate wastewater systems, the conversion of NO₃[−] to NH₃ is constrained by sluggish water dissociation kinetics and weak NO₃[−] adsorption. Recently, dual-active-site catalysts have attracted increasing attention for the electrochemical NitRR.^{22,23} Previous studies have demonstrated that transition metals with high electrical conductivity and platinum-like electronic structures can efficiently generate adsorbed hydrogen through water dissociation, thereby promoting nitrate reduction.^{24,25} Furthermore, theoretical calculations indicate that iron (Fe) atoms exhibit low energy barriers for nitrogen–oxygen intermediates (e.g., *NO₂, *NO), resulting in high selectivity toward NH₃.^{26,27} However, Fe-based catalysts show limited affinity for nitrate adsorption, which hinders the

^aKey Laboratory of Materials Physics, Centre for Environmental and Energy Nanomaterials, Anhui Key Laboratory of Nanomaterials and Nanotechnology, CAS Center for Excellence in Nanoscience Institute of Solid State Physics, HFSIP, Chinese Academy of Sciences, Hefei 230031, China. E-mail: shbzhang@issp.ac.cn, zhanghm@issp.ac.cn

^bUniversity of Science and Technology of China, Hefei 230026, China



initial reduction of NO_3^- to NO_2^- and promotes the competing hydrogen evolution reaction (HER).^{26,27} Copper (Cu) atoms, whose d-orbitals exhibit favorable energy alignment with the π^* orbitals of nitrate, enhance both the adsorption and reduction of NO_3^- to NO_2^- .^{25,28} Therefore, incorporating Cu atoms into Fe-based catalysts can provide sufficient NO_2^- intermediates for the subsequent deoxygenation and hydrogenation steps. Based on a basic electrochemical property analysis of Cu and Fe, we anticipate that the Cu–Fe-based dual-site catalyst will significantly improve NitRR performance under ambient conditions.

In this study, we propose a Cu–Fe dual-site synergistic catalytic mechanism, in which CuO is introduced into Fe_3O_4 to enhance NO_3^- adsorption and conversion at the Cu site, while optimizing *H adsorption at the Fe site, thereby achieving significantly improved NitRR performance. Intriguingly, during the initial stage of electrolysis, the pre-loaded CuO nanoparticles were partially reduced, forming rod-like metallic copper (Cu). Concurrently, the outer layer of the Fe_3O_4 phase underwent oxidation to Fe_2O_3 . The resulting Cu and CuO species worked together as the copper active sites, while the Fe_2O_3 and Fe_3O_4 phases collectively functioned as the iron-based active sites. The CuO– Fe_3O_4 dual-site demonstrated outstanding performance, achieving an NH_3 yield rate of $39.2 \pm 3.5 \text{ mg h}^{-1} \text{ mg}_{\text{cat}}^{-1}$ and a faradaic efficiency of $90.5 \pm 2.2\%$ at -0.8 V (vs. RHE). ^{15}N isotopic labelling experiments were conducted to verify the nitrogen source of the synthesized NH_3 , with quantification performed using the colorimetric method. *In situ* attenuated total reflectance surface-enhanced infrared absorption spectroscopy (ATR-SEIRAS) revealed that the CuO– Fe_3O_4 dual site exhibits exclusive selectivity for NH_3 during the electrocatalytic NitRR, which was further unveiled by *in situ* differential electrochemical mass spectrometry (DEMS) analysis.

Fig. 1a depicts a schematic representation of the synthesis process employed for synthesizing the CuO– Fe_3O_4 dual site supported on carbon nanotubes (CuO– Fe_3O_4 /CNTs) *via* a simple two-step method of impregnation adsorption and high-temperature calcination. The actual loading amounts of Cu and Fe in the CuO– Fe_3O_4 /CNTs catalyst are 26.0% and 11.4%, respectively, by inductively coupled plasma atomic emission spectroscopy (ICP-AES). For comparison, CuO and Fe_3O_4 single sites anchored on the CNTs (CuO/CNTs and Fe_3O_4 /CNTs) with Cu and Fe loadings of 32.3% and 30.6% were also synthesized through a similar synthetic process to that for CuO– Fe_3O_4 /CNTs (Fig. S1, SI). Fig. 1b presents the X-ray diffraction (XRD) pattern of the CuO– Fe_3O_4 /CNTs sample. The strong peak at 26.1° matches the characteristic signal of carbon (JCPDS card 97-002-8419), which is attributed to the highly graphitized carbon nanotube (CNT) substrate.²⁹ Additional peaks at approximately 32.7° , 38.6° , 49.9° , 53.4° , 61.6° , 65.8° and 74.1° correspond to the $(1\ 1\ 0)$, $(1\ 1\ 1)$, $(-2\ 0\ 2)$, $(0\ 2\ 0)$, $(-1\ 1\ 3)$, $(1\ 1\ 3)$ and $(0\ 0\ 4)$ planes of CuO (JCPDS no. 44-0706).³⁰ Meanwhile, the characteristic peaks at 30.01° , 35.26° , 36.73° , 43.24° , 57.01° , and 62.75° match the $(2\ 2\ 0)$, $(3\ 1\ 1)$, $(2\ 2\ 2)$, $(4\ 0\ 0)$, $(5\ 1\ 1)$, and $(4\ 4\ 0)$ planes of cubic Fe_3O_4 (JCPDS no. 00-0629),³¹ respectively, which confirms the existence of Fe species in the form of oxides in the Fe_3O_4 /CNTs catalyst. The microscopic morphology of CuO– Fe_3O_4 /CNTs was characterized *via* scanning electron microscopy (SEM) (Fig. S2, SI). In the SEM images, the CNTs substrate could be clearly discerned (Fig. S3, SI). The CNTs presented a clear cylindrical tubular structure, with CuO and Fe_3O_4 nanoparticles deposited on its surface. As depicted in Fig. S3 (SI), at the microstructural scale, the CNTs were stacked and randomly dispersed. This arrangement not only enhanced the conductivity of the catalyst but also provided an abundance of active sites.³² The hollow tubular structure and open pores of the CNTs facilitated the diffusion of reactants and products, thus improving the mass transfer efficiency in liquid-phase reactions. Moreover, the transmission electron microscopy (TEM) image of CuO– Fe_3O_4 /

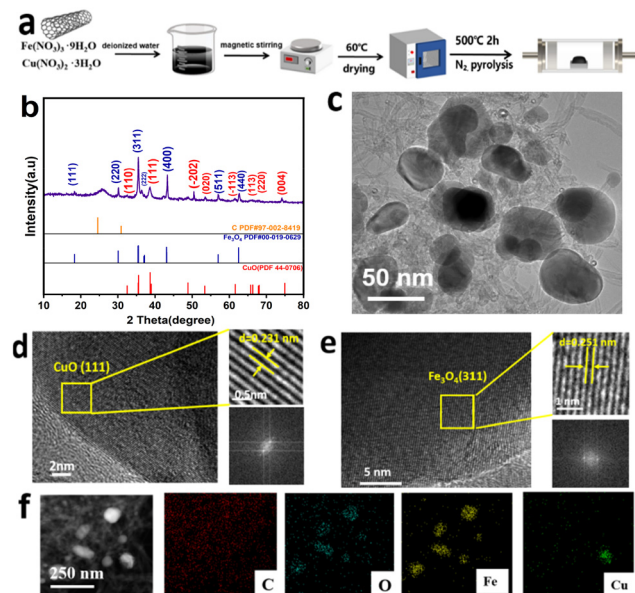


Fig. 1 (a) Schematic illustration of the synthetic process of the CuO– Fe_3O_4 /CNTs sample. (b) XRD pattern of CuO– Fe_3O_4 /CNTs. (c) TEM image of CuO– Fe_3O_4 /CNTs. (d) and (e) HR-TEM images of CuO– Fe_3O_4 /CNTs (f) EDX mapping images of CuO– Fe_3O_4 /CNTs.

019-0629),³¹ respectively, which confirms the existence of Fe species in the form of oxides in the Fe_3O_4 /CNTs catalyst. The microscopic morphology of CuO– Fe_3O_4 /CNTs was characterized *via* scanning electron microscopy (SEM) (Fig. S2, SI). In the SEM images, the CNTs substrate could be clearly discerned (Fig. S3, SI). The CNTs presented a clear cylindrical tubular structure, with CuO and Fe_3O_4 nanoparticles deposited on its surface. As depicted in Fig. S3 (SI), at the microstructural scale, the CNTs were stacked and randomly dispersed. This arrangement not only enhanced the conductivity of the catalyst but also provided an abundance of active sites.³² The hollow tubular structure and open pores of the CNTs facilitated the diffusion of reactants and products, thus improving the mass transfer efficiency in liquid-phase reactions. Moreover, the transmission electron microscopy (TEM) image of CuO– Fe_3O_4 /

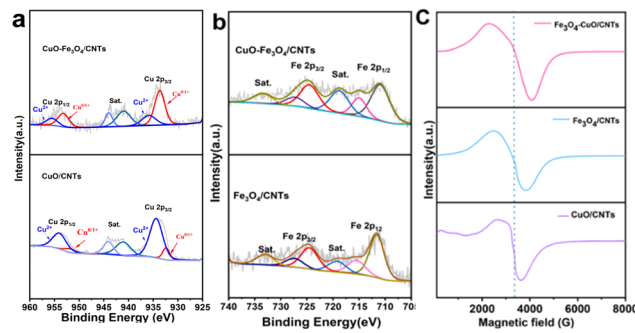


Fig. 2 (a) The Cu 2p XPS spectra of the different catalysts. (b) Fe 2p spectra of the different samples. (c) EPR spectroscopy of the different catalysts.

CNTs (Fig. 2c) further demonstrated that CuO and Fe_3O_4 were firmly anchored on the CNTs. The high-resolution transmission electron microscopy (HR-TEM) images (Fig. 2d and e) exhibit lattice fringes measuring 0.251 nm and 0.231 nm. These lattice fringes correspond to the (3 1 1) plane of Fe_3O_4 and the (1 1 1) plane of CuO, respectively, which is in good agreement with the XRD results. Additionally, high-angle annular dark-field scanning transmission electron microscopy (HAADF-STEM) and the corresponding energy-dispersive X-ray (EDX) mapping images (Fig. 2f) reveal that the elements Cu, Fe, C, and O are homogeneously distributed on the carbon nanotubes. The N_2 adsorption–desorption isotherm measurement results (Fig. S4, SI) reveal that the BET surface area of $\text{CuO-Fe}_3\text{O}_4/\text{CNTs}$ is $178.8 \text{ m}^2 \text{ g}^{-1}$. The sample displays a typical type IV isotherm with distinct hysteresis loops, which indicates the existence of mesoporous structures, and the pore volume is $0.82 \text{ cm}^3 \text{ g}^{-1}$. The high surface area and porous architecture of this catalyst are conducive to charge and mass transport during electrocatalytic processes.³²

To further investigate the surface elemental composition and valence states, X-ray photoelectron spectroscopy (XPS) was carried out on $\text{CuO-Fe}_3\text{O}_4/\text{CNTs}$, CuO/CNTs, and $\text{Fe}_3\text{O}_4/\text{CNTs}$ samples. Fig. S5a (SI) presents the survey spectra of $\text{CuO-Fe}_3\text{O}_4/\text{CNTs}$, confirming the presence of C, O, Fe, and Cu elements. The O 1s spectrum (Fig. S5c, SI) shows a peak at 531.7 eV attributed to oxygen vacancies (V_O), and another at 530.3 eV corresponding to Fe–O bonds.^{33,34} The superior nitrate reduction activity observed for the $\text{CuO-Fe}_3\text{O}_4/\text{CNTs}$ catalyst can be attributed in part to its high concentration of oxygen vacancies, as confirmed by electron paramagnetic resonance (EPR) spectroscopy (Fig. 2c). All samples exhibited a characteristic EPR signal at a *g*-value of 2.002, which is associated with unpaired electrons located at oxygen vacancy sites.³⁵ Notably, the $\text{CuO-Fe}_3\text{O}_4/\text{CNTs}$ composite showed the highest signal intensity, indicating a greater abundance of oxygen vacancies compared to the other catalysts. The slanted baseline of the EPR spectra, a common feature in magnetic materials, was appropriately corrected during data analysis. These oxygen vacancies play an essential role in enhancing catalytic performance by modulating the surface electronic structure, which facilitates electron transfer to adsorbed nitrate ions and strengthens their interaction with the catalyst surface, thereby significantly promoting the reduction activity.^{36,37} In the Cu 2p spectrum (Fig. 2a), the peaks for CuO/CNTs are mainly associated with Cu^{2+} , while those for $\text{Cu}^{0/1+}$ are relatively weak. Upon integration with Fe_3O_4 , a notable electronic modulation of Cu species is observed, as reflected in the shifts in Cu 2p peaks. Specifically, the $\text{Cu}^{0/1+}$ states ($2p_{3/2}$: 933.7 eV, $2p_{1/2}$: 953.3 eV) show significantly enhanced intensity, whereas the Cu^{2+} signals ($2p_{3/2}$: 936.0 eV, $2p_{1/2}$: 955.7 eV) are attenuated.^{30,38} This decrease in the $\text{Cu}^{2+}/\text{Cu}^0$ ratio indicates electron transfer from Fe_3O_4 to CuO centers, which is further confirmed by the results of differential charge analysis (Fig. S6, SI). The Fe 2p spectrum (Fig. 2b) reveals two pairs of peaks at ~ 710.6 eV and ~ 723.6 eV, as well as ~ 714.7 eV and ~ 726.4 eV, which correspond to the Fe 2p_{3/2}

and Fe 2p_{1/2} peaks of Fe^{2+} and Fe^{3+} , respectively.³³ The high-resolution C 1s spectrum (Fig. S5b, SI) can be deconvoluted into three components at 284.8 eV (C–C), 286.7 eV (C–O), and 289.7 eV (O=C–O).³⁹

The NitRR performance of all as-prepared catalysts was evaluated using an electrochemical workstation in an H-type electrolytic cell under ambient temperature and pressure. First, the NitRR electrochemical performance was assessed by linear sweep voltammetry (LSV). Prior to each test, cyclic voltammetry (CV) scans were conducted until the polarization curves stabilized. The concentrations of NH_3 and the by-product NO_2^- were determined *via* colorimetric analysis. The corresponding calibration curves are presented in Fig. S7–S9 (SI). As shown in Fig. 3a, the LSV curve of $\text{CuO-Fe}_3\text{O}_4/\text{CNTs}$ in 0.1 M KOH with nitrate exhibits a significantly higher current density compared to that without nitrate, indicating nitrate participation in the electrochemical reaction. Similarly, the LSV curves of CuO/CNTs and $\text{Fe}_3\text{O}_4/\text{CNTs}$ (Fig. 3b) show the same trend; however, their current densities are notably lower than that of $\text{CuO-Fe}_3\text{O}_4/\text{CNTs}$, suggesting a synergistic effect between CuO and Fe_3O_4 in promoting nitrate reduction. With respect to onset potential, CuO/CNTs and $\text{CuO-Fe}_3\text{O}_4/\text{CNTs}$ exhibit similar values, indicating that CuO plays a key role in nitrate adsorption and activation.

To further demonstrate its superior electrochemical performance, chronoamperometry (*i*–*t*) was conducted at applied

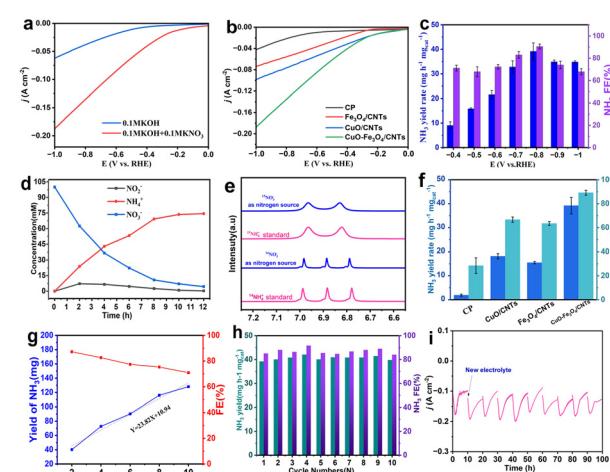


Fig. 3 (a) LSV curves of $\text{CuO-Fe}_3\text{O}_4/\text{CNTs}$ in Ar-saturated 0.1 M KOH with and without nitrate. (b) LSV curves of the CP, $\text{CuO-Fe}_3\text{O}_4/\text{CNTs}$, $\text{Fe}_3\text{O}_4/\text{CNTs}$ and CuO/CNTs for nitrate reduction in 0.1 M KOH electrolyte containing 0.1 M KNO_3 . (c) NH_3 yield rate and FE of the $\text{CuO-Fe}_3\text{O}_4/\text{CNTs}$ catalyst obtained at different applied potentials. (d) Concentration changes of NO_3^- , NO_2^- , NH_3 of $\text{CuO-Fe}_3\text{O}_4/\text{CNTs}$ at -0.8 V (vs. RHE). (e) ^1H NMR spectra of $^{14}\text{NH}_4^+$ and $^{15}\text{NH}_4^+$ standards, and the resultant samples from $\text{CuO-Fe}_3\text{O}_4/\text{CNTs}$ -catalyzed NitRR using $^{14}\text{NO}_3^-$ and $^{15}\text{NO}_3^-$ as nitrogen source, respectively. (f) Ammonia yield rate and faradaic efficiencies of CP, CuO/CNTs, $\text{Fe}_3\text{O}_4/\text{CNTs}$, and $\text{CuO-Fe}_3\text{O}_4/\text{CNTs}$ at -0.8 V (vs. RHE). (g) The NH_3 yield and FE for NH_3 production over $\text{CuO-Fe}_3\text{O}_4/\text{CNTs}$ toward electrocatalytic NitRR with reaction time at -0.8 V (vs. RHE). (h) Cycling stability test of $\text{CuO-Fe}_3\text{O}_4/\text{CNTs}$ at -0.8 V (vs. RHE) for 10 cycles. (i) The *i*–*t* curve of long-term stability test for 100 h at -0.8 V (vs. RHE).

potentials ranging from -0.4 to -1.0 V (vs. RHE) to determine the ammonia yield rate and Faraday efficiency (Fig. S10, SI). The corresponding NH_3 yield rate (R_{NH_3}) and Faraday efficiency (FE) under these potentials are shown in Fig. 3c. Both R_{NH_3} and FE exhibit a volcano-shaped dependence on potential, peaking at -0.8 V (vs. RHE), likely due to competition with the hydrogen evolution reaction. Notably, $\text{CuO-Fe}_3\text{O}_4/\text{CNTs}$ achieves an impressive R_{NH_3} of $39.2 \pm 3.5 \text{ mg h}^{-1} \text{ mg}_{\text{cat.}}^{-1}$ and a high FE of $90.5 \pm 2.2\%$ at -0.8 V (vs. RHE) in $0.1 \text{ M KOH} + 0.1 \text{ M KNO}_3$, outperforming most previously reported NitRR electrocatalysts (Table S1, SI). Importantly, NH_3 is the dominant product, with minimal NO_2^- detected in the final solution (Fig. S11, SI), indicating excellent selectivity for the NitRR. Fig. 3d presents the concentration–time profiles of NH_3 , NO_3^- , and NO_2^- . The continuous decrease in NO_3^- and increase in NH_3 confirm that nitrate is steadily converted into ammonia. Meanwhile, the initial rise followed by a decline in NO_2^- suggests that it is an intermediate species subsequently reduced to NH_3 . The ^1H NMR spectra of the standards and the $^{14}\text{NH}_4^+$ and $^{15}\text{NH}_4^+$ produced in the NitRR samples (Fig. 3e) confirm that the generated NH_3 originates from the 0.1 M KNO_3 feedstock. Additionally, the amount of $^{15}\text{NH}_3$ was quantified using the indophenol blue method, yielding results consistent with those for $^{14}\text{NH}_3$ at -0.8 V (vs. RHE) (Fig. S12, SI).

Furthermore, the NitRR activity of the four catalysts was evaluated at -0.8 V (vs. RHE), as shown in Fig. 3f. The NH_3 faradaic efficiencies of $\text{CuO-Fe}_3\text{O}_4/\text{CNTs}$, CuO/CNTs , $\text{Fe}_3\text{O}_4/\text{CNTs}$, and CP were 90.5% , 66.7% , 63.5% , and 28.4% , respectively. It is also worth noting that the ammonia yield of $\text{CuO-Fe}_3\text{O}_4/\text{CNTs}$ is $39.2 \text{ mg h}^{-1} \text{ mg}_{\text{cat.}}^{-1}$, which is 2.2 times that of CuO/CNTs ($18.2 \text{ mg h}^{-1} \text{ mg}_{\text{cat.}}^{-1}$), 2.65 times that of $\text{Fe}_3\text{O}_4/\text{CNTs}$ ($15.5 \text{ mg h}^{-1} \text{ mg}_{\text{cat.}}^{-1}$), and 20.6 times that of CNTs ($1.9 \text{ mg h}^{-1} \text{ mg}_{\text{cat.}}^{-1}$). It is confirmed that the superior NitRR performance of $\text{CuO-Fe}_3\text{O}_4/\text{CNTs}$ comes from the synergistic effect of CuO and Fe_3O_4 in the catalyst. Additionally, the durability of $\text{CuO-Fe}_3\text{O}_4/\text{CNTs}$ for 12 hours at -0.8 V (vs. RHE) was confirmed by chronoamperometry measurements (Fig. S13, SI). The obtained NH_3 yield and reaction time show a linear relationship, with a slight decrease in FE (Fig. 3g), demonstrating the excellent stability of $\text{CuO-Fe}_3\text{O}_4/\text{CNTs}$. At the same time, $\text{CuO-Fe}_3\text{O}_4/\text{CNTs}$ also demonstrated good catalytic stability, with only minor variations in FE observed over ten cycles (Fig. 3h).

The long-term stability of a catalyst is a critical indicator for assessing its practical applicability. As demonstrated in Fig. 3i, a 100-hour durability test was conducted on the $\text{CuO-Fe}_3\text{O}_4/\text{CNTs}$ catalyst, with the electrolyte replenished every 10 hours. After each refresh, the current density, that had increased during the reaction, returned to its original level, indicating good stability. SEM characterization further confirmed the structural robustness of the material. Comparisons among the post-reaction samples after 100 hours (Fig. S14a, SI), 10 cycles (20 hours, Fig. S14b, SI), and the fresh catalyst (Fig. S2, SI), revealed no significant morphological changes in the carbon nanotubes. The CNT network remained intact without apparent change, underscoring the essential role of the CNT frame-

work in providing mechanical support and electrical conductivity throughout the prolonged test. Notably, phase transformations occurred within the CuO and Fe_3O_4 ; some of the initially loaded CuO nanoparticles were reduced to metallic Cu, forming nanorod-like structures (Fig. S14c, SI) as indicated by the lattice fringes of the (111) plane of Cu in Fig. S14d (SI). Simultaneously, the surface of the Fe_3O_4 particles was oxidized to Fe_2O_3 , which was identified by the lattice spacing corresponding to the (104) plane of Fe_2O_3 (Fig. S14e, SI).

Crucially, the chemical state analysis *via* XPS, which we conducted on the catalyst after 10 continuous cycles of operation, already provides definitive evidence of reconstruction. As illustrated in Fig. S15a (SI), the Cu 2p spectrum exhibits a negative binding energy shift along with an increased ratio of Cu^0/Cu^+ to Cu^{2+} , indicating electron transfer from Fe_3O_4 to CuO during the reaction. Correspondingly, the Fe 2p spectrum (Fig. S15b, SI) shows a decreased $\text{Fe}^{2+}/\text{Fe}^{3+}$ ratio and the disappearance of satellite features, confirming the oxidation of Fe_3O_4 to Fe_2O_3 within 20 hours. These findings not only verify the electron transfer between CuO and Fe_3O_4 ,³⁵ but also demonstrate that *in situ* reconstruction occurs rapidly within the initial hours of operation. Also, the coexistence of CuO and Fe_3O_4 accelerates electron transfer from the Fe component to the Cu component, which enhances the adsorption/activation of nitrate on the negative Cu sites and the affinity of atomic hydrogen on the positive Fe sites. It thus significantly improves the intrinsic catalytic activity of the catalyst by a synergistic effect.

To confirm that the produced NH_3 originates from the electrocatalytic nitrate reduction reaction (NitRR) on $\text{CuO-Fe}_3\text{O}_4/\text{CNTs}$, two control experiments were conducted: (i) in 0.1 M KOH electrolyte, and (ii) in $0.1 \text{ M KOH} + 0.1 \text{ M KNO}_3$ electrolyte under open-circuit conditions (Fig. 4a). In both cases, only negligible amounts of NH_3 were detected. To compare the intrinsic activities of the catalysts, electrochemical active surface areas (ECSAs) were evaluated. The double-layer capacitance (C_{dl}) was determined from cyclic voltammetry measurements at scan rates ranging from 20 to 160 mV s^{-1} (Fig. 4b and Fig. S16, SI). Based on these values, the ECSA of $\text{CuO-Fe}_3\text{O}_4/\text{CNTs}$ was calculated to be 336.25 cm^{-2} , which is larger than those of CuO/CNTs (224.25 cm^{-2}) and $\text{Fe}_3\text{O}_4/\text{CNTs}$ (264.25 cm^{-2}), indicating a greater number of accessible electrocatalytic active sites (Fig. 4c).

The ultimate goal of nitrate reduction (NO_3RR) also encompasses the practical removal of nitrate from wastewater. As real industrial effluents often contain nitrate at low concentrations under near-neutral pH conditions, we further evaluated the catalyst using a 1000 ppm NO_3^- solution (16.1 mM) in $0.1 \text{ M K}_2\text{SO}_4$ electrolyte to better simulate such environments. The $i-t$ curve exhibited outstanding stability throughout the 15-hour test, showing only minor fluctuations and underscoring the structural robustness and operational stability of the catalyst under realistic wastewater conditions (Fig. 4d). Following electrolysis, the remaining nitrate concentration was quantified using UV-vis spectroscopy (Fig. 4e), revealing a final concentration of 34.36 ppm (Fig. 4f), which is well below the 50 ppm



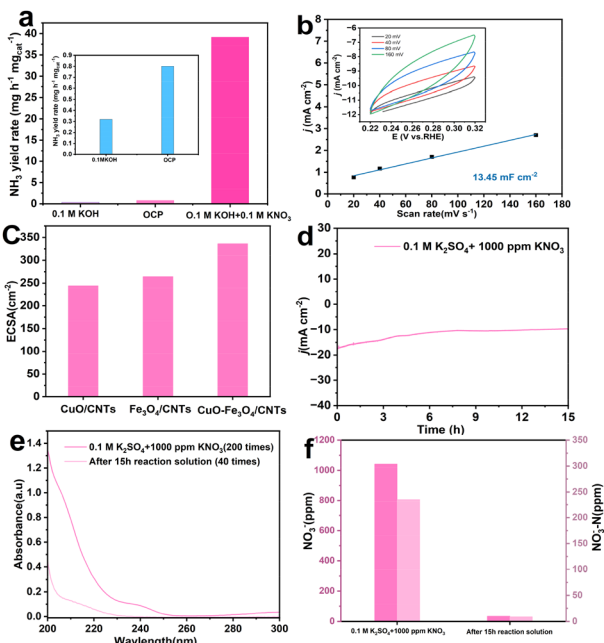


Fig. 4 (a) Comparison of ammonia contents of $\text{CuO-Fe}_3\text{O}_4/\text{CNTs}$ and the black control groups under alkaline conditions (inset is an enlarged image of the control groups). (b) Plots of current density *versus* scan rate for $\text{CuO-Fe}_3\text{O}_4/\text{CNTs}$ catalysts, the inset CV curves in $0.1 \text{ M KOH} + 0.1 \text{ M KNO}_3$ electrolyte at different scan rates. (c) ESCA of different catalysts. (d) The i - t curve of 15 h in $0.1 \text{ M K}_2\text{SO}_4 + 1000 \text{ ppm KNO}_3$. (e) UV-vis spectra of the nitrate solution before and after a 15 h electrolysis process in $0.1 \text{ M K}_2\text{SO}_4 + 1000 \text{ ppm KNO}_3$. (f) The corresponding NO_3^- concentration calculated based on (e).

NO_3^- limit established by the World Health Organization (WHO) for drinking water. This result confirms the role of the catalyst in reducing nitrate concentrations to levels compliant with international safety standards.

In situ attenuated total reflectance surface-enhanced infrared absorption spectroscopy (ATR-SEIRAS) was employed to investigate the reaction intermediates during the nitrate reduction reaction (NitRR). The experimental setup and cell configuration are shown in Fig. 5a. Fig. 5b displays the infrared spectra obtained during the negative potential scan from -0.4 to -1.0 V (vs. RHE) on $\text{CuO-Fe}_3\text{O}_4/\text{CNTs}$. A band at 1592 cm^{-1} is attributed to the N-O vibration of adsorbed NO in a bridge configuration at the open circuit potential (OCP).^{40,41} As the potential increases, a weak absorption band at 1357 cm^{-1} appears, corresponding to the asymmetric N-O stretching vibration of NO_3^- ,^{19,41} indicating NO_3^- consumption during the reaction. Meanwhile, a signal at 1288 cm^{-1} is assigned to the wagging mode of $-\text{NH}_2$, a key intermediate in ammonia formation.⁴² Importantly, a gradually enhanced band at 1440 cm^{-1} corresponds to the N-H bending vibration of NH_3 , providing direct evidence for ammonia production.⁴³⁻⁴⁵ In addition, *in situ* differential electrochemical mass spectrometry (DEMS) was conducted to detect gaseous intermediates and products. Fig. 5c shows the m/z signals at 14, 15, 16, 17, 30, 31, 32, 33, and 46, which are

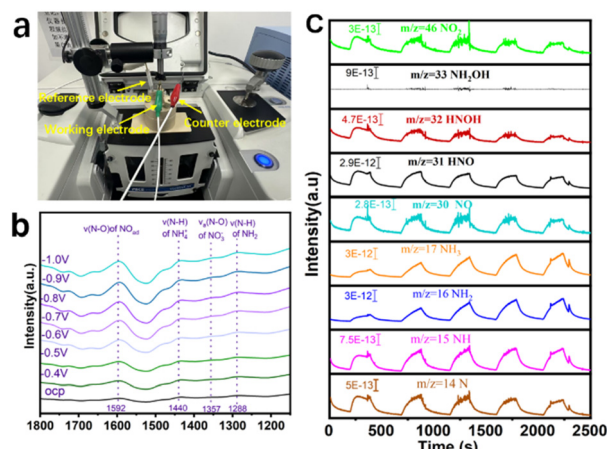


Fig. 5 (a) Physical photograph of *in situ* ATR-SEIRAS reactor for (b) *in situ* ATR-SEIRAS spectra of electrocatalytic NitRR on $\text{CuO-Fe}_3\text{O}_4/\text{CNTs}$ at different potentials in the $0.1 \text{ M KOH} + 0.1 \text{ M KNO}_3$ electrolyte. (c) *in situ* DEMS measurements for $\text{CuO-Fe}_3\text{O}_4/\text{CNTs}$ in the $0.1 \text{ M KOH} + 0.1 \text{ M KNO}_3$ electrolyte at -0.8 V (vs. RHE) for the NitRR.

assigned to N, NH, NH_2 , NH_3 , NO, HNO, HNOH, NH_2OH , and NO_2 , respectively. Compared to other intermediates, the strongest NH_3 signal confirms the high selectivity of $\text{CuO-Fe}_3\text{O}_4/\text{CNTs}$ for ammonia production. Notably, no NH_2OH intermediate was detected. Based on the *in situ* ATR-SEIRAS and DEMS results, the following NitRR pathway on $\text{CuO-Fe}_3\text{O}_4/\text{CNTs}$ is proposed: $\text{NO}_3^- \rightarrow \text{NO}_3^* \rightarrow \text{NO}_2^* \rightarrow \text{NO}^* \rightarrow \text{HNO}^* \rightarrow \text{HNOH}^* \rightarrow \text{N}^* \rightarrow \text{NH}^* \rightarrow \text{NH}_2^* \rightarrow \text{NH}_3^* \rightarrow \text{NH}_3$. These *in situ* spectroscopic findings provide strong evidence for the successful synthesis of NH_3 *via* the NitRR, supporting the previously reported electrocatalytic performance.

Leveraging the eight-electron transfer process for nitrate-to-ammonia conversion and the high energy density of ammonia, we constructed a rechargeable Zn-NO_3^- battery system. As illustrated in Fig. 6a, the battery employs a Zn foil anode and a $\text{CuO-Fe}_3\text{O}_4/\text{CNTs}$ cathode for electrocatalytic nitrate reduction (NitRR). This system not only delivers electrical power but also enables simultaneous ammonia synthesis and wastewater purification. The open-circuit voltage (OCV) of the Zn-NO_3^- battery with the $\text{CuO-Fe}_3\text{O}_4/\text{CNTs}$ cathode reached approximately 1.54 V vs. Zn (Fig. 6b). Notably, the battery achieved a maximum power density of 11.21 mW cm^{-2} (Fig. 6c), surpassing values reported in previous studies.^{46,47} To evaluate its practical power supply capability, the battery was used to drive a commercial electronic timer (typically powered by a 1.5 V dry battery), sustaining operation continuously for 99 minutes (Fig. 6d). During discharge, the anodic dissolution of Zn drives the nitrate reduction reaction (NitRR) at the $\text{CuO-Fe}_3\text{O}_4/\text{CNTs}$ cathode. The battery exhibited a stable discharge profile, with gradually decreasing potential and steadily increasing current output. This result remained consistent across multiple current densities, highlighting its superior discharge performance (Fig. 6e). To further confirm the dual functionality of the Zn-NO_3^- battery, including co-producing ammonia and elec-

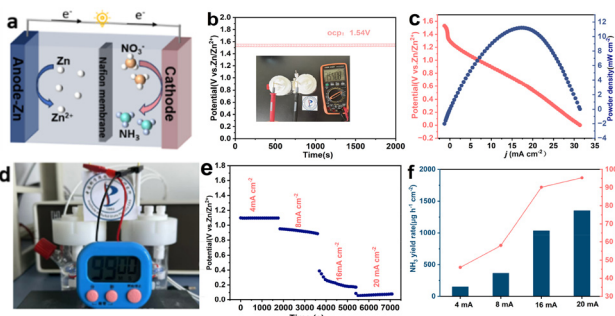


Fig. 6 (a) Schematic illustration of the $\text{Zn}-\text{NO}_3^-$ battery assembled with the $\text{CuO}-\text{Fe}_3\text{O}_4/\text{CNTs}$ cathode. (b) OCV curve of the $\text{Zn}-\text{NO}_3^-$ battery assembled with the $\text{CuO}-\text{Fe}_3\text{O}_4/\text{CNTs}$ cathode. Inset of (b) showing a photograph of the OCV measurement of the $\text{Zn}-\text{NO}_3^-$ battery. (c) Discharging curves and the corresponding power density plot. (d) Digital photos of the electronic timer powered by this $\text{Zn}-\text{NO}_3^-$ battery. (e) Discharging tests at different current densities of this $\text{Zn}-\text{NO}_3^-$ battery. (f) NH_3 FE and NH_3 yield rates in the discharge process (we assembled a rechargeable $\text{Zn}-\text{NO}_3^-$ battery using highly active $\text{CuO}-\text{Fe}_3\text{O}_4/\text{CNTs}$ as the cathode).

tricity, the faradaic efficiency of ammonia (FE_{NH_3}) and the NH_3 yield rate were measured under increasing current densities (Fig. 6f). At current densities up to 20 mA cm^{-2} , the system achieved a high FE_{NH_3} of 95.4% and an NH_3 production rate of $1351.4 \text{ }\mu\text{g h}^{-1} \text{ cm}^{-2}$. These results underscore the promising potential of $\text{CuO}-\text{Fe}_3\text{O}_4/\text{CNTs}$ as an efficient cathode material for $\text{Zn}-\text{NO}_3^-$ batteries in the fields of energy storage and conversion.

In conclusion, the $\text{CuO}-\text{Fe}_3\text{O}_4$ dual-site catalyst is experimentally proved to be a superb NitRR electrocatalyst for ambient NH_3 production with a large yield of $39.2 \pm 3.5 \text{ mg h}^{-1} \text{ mg}_{\text{cat}}^{-1}$ and a faradaic efficiency of $90.5 \pm 2.2\%$ at -0.8 V (vs. RHE). Distinct from conventional static catalysts, the $\text{CuO}-\text{Fe}_3\text{O}_4/\text{CNTs}$ material experiences dynamic reconstruction under reaction conditions, giving rise to a hybrid structure consisting of Cu/CuO and $\text{Fe}_2\text{O}_3/\text{Fe}_3\text{O}_4$. This self-optimizing property offers a promising framework for the design of catalysts featuring higher activity and longer-term stability. *In situ* ATR-SEIRAS and DEMS analysis was employed to identify the intermediate produced during the electrocatalytic NitRR process, confirming $\text{CuO}-\text{Fe}_3\text{O}_4/\text{CNTs}$ as a promising electrocatalyst for NH_3 synthesis. The results indicate that the Cu-Fe dual-site enhances the adsorption of NO_3^- and ${}^*\text{H}$, thereby improving the reaction kinetics of the NitRR under ambient conditions. However, clarifying the underlying mechanism through more detailed and direct *in situ* experimental studies is the key direction for future work. Moreover, the zinc-nitrate battery equipped with the $\text{CuO}-\text{Fe}_3\text{O}_4/\text{CNTs}$ cathode can simultaneously achieve power generation and ammonia production, with a power density of 11.21 mW cm^{-2} and a high faradaic efficiency of ammonia of 95.4% in 20 mA cm^{-2} . These results highlight the crucial role of electrochemical reconfiguration and the synergistic effect between CuO and Fe_3O_4 , providing an effective strategy for the rational design of high-performance electrocatalysts for nitrate reduction.

Author contributions

Shun Zhang: conceptualization, investigation, visualization, writing – original draft. Shengbo Zhang: data curation, resources, writing – review & editing. Jiafang Liu: investigation, resources. Zhixian Mao: investigation. Yunxia Zhang: supervision. Guozhong Wang: supervision. Huajie Yin: supervision. Haiming Zhang: funding acquisition, supervision, resources, writing – review & editing.

Conflicts of interest

There are no conflicts to declare.

Data availability

The data supporting this article have been included as part of the supplementary information (SI). Supplementary information including differential charge analysis of $\text{CuO}-\text{Fe}_3\text{O}_4/\text{CNTs}$, SEM, TEM of $\text{CuO}-\text{Fe}_3\text{O}_4/\text{CNTs}$ after 100 h stability test and others is available. See DOI: <https://doi.org/10.1039/d5qi01543j>.

Acknowledgements

This work was financially supported by the Natural Science Foundation of China (Grant No. 52502124 and 52472113) and the Anhui Provincial Natural Science Foundation (Grant No. 2408085MB021). We thank the staff members of the Electron Spin Resonance System (<https://cstr.cn/31125.02.SHMFF.ESR>) at the Steady High Magnetic Field Facility, CAS (<https://cstr.cn/31125.02.SHMFF>), for providing technical support and assistance in data collection and analysis.

References

- 1 G.-F. Chen, Y. Yuan, H. Jiang, S.-Y. Ren, L.-X. Ding, L. Ma, T. Wu, J. Lu and H. Wang, Electrochemical reduction of nitrate to ammonia via direct eight-electron transfer using a copper-molecular solid catalyst, *Nat. Energy*, 2020, **5**, 605–613.
- 2 N. Gruber and J. N. Galloway, An earth-system perspective of the global nitrogen cycle, *Nature*, 2008, **451**, 293–296.
- 3 R. F. Service, New recipe produces ammonia from air, water, and sunlight, *Science*, 2014, **345**, 610–610.
- 4 G. Soloveichik, Electrochemical synthesis of ammonia as a potential alternative to the Haber–Bosch process, *Nat. Catal.*, 2019, **2**, 377–380.
- 5 J. C. Li, M. Li, N. An, S. Zhang, Q. A. Song, Y. L. Yang, J. Li and X. Liu, Boosted ammonium production by single cobalt atom catalysts with high Faradic efficiencies, *Proc. Natl. Acad. Sci. U. S. A.*, 2022, **119**, e2123450119.



6 B. H. R. Suryanto, H.-L. Du, D. Wang, J. Chen, A. N. Simonov and D. R. MacFarlane, Challenges and prospects in the catalysis of electroreduction of nitrogen to ammonia, *Nat. Catal.*, 2019, **2**, 290–296.

7 C. Guo, J. Ran, A. Vasileff and S. Qiao, Rational design of electrocatalysts and photo(electro)catalysts for nitrogen reduction to ammonia (NH_3) under ambient conditions, *Energy Environ. Sci.*, 2018, **11**, 45–56.

8 Z.-X. Yin, Y.-D. Li, Y.-H. Ye, Y. Liu, M.-F. Li, Z.-J. Yang, X.-R. Zheng, H.-Z. Wang, Y. Wang and Y.-D. Deng, Sp/sp² carbon ratio-driven high-throughput screening of electrocatalytic nitrogen reduction performance on transition metal single-atom catalysts, *Rare Met.*, 2024, **43**, 5781–5791.

9 S. Choe, N. Kim and Y. J. Jang, Perspective on the interfacial engineering for electrocatalytic N_2 to NH_3 conversion from catalysts to systems, *EcoEnergy*, 2023, **1**, 3–15.

10 Y.-H. Cui, W.-C. Ouyang, A.-J. Gao, C.-Y. Yu and L.-P. Zhang, Promoting electrocatalytic nitrogen reduction to ammonia via dopant boron on two-dimensional materials, *Rare Met.*, 2024, **43**, 5117–5125.

11 Y. Tan, Y. Zhao, X. Chen, S. Zhai, X. Wang, L. Su, H. Yang, W. Deng, G. W. Ho and H. Wu, Cooperative Cu with defective MXene for enhanced nitrate electroreduction to ammonia, *EcoEnergy*, 2024, **2**, 258–267.

12 K. Wang, R. Mao, R. Liu, J. Zhang, H. Zhao, W. Ran and X. Zhao, Intentional corrosion-induced reconstruction of defective NiFe layered double hydroxide boosts electrocatalytic nitrate reduction to ammonia, *Nat. Water*, 2023, **1**, 1068–1078.

13 X. Zhang, X. Liu, Z.-F. Huang, L. Gan, S. Zhang, R. Jia, M. Ajmal, L. Pan, C. Shi, X. Zhang, G. Yang and J. J. Zou, Regulating intermediate adsorption and H_2O dissociation on a diatomic catalyst to promote electrocatalytic nitrate reduction to ammonia, *Energy Environ. Sci.*, 2024, **17**, 6717–6727.

14 W. Wen, S. Fang, Y. Zhou, Y. Zhao, P. Li and X. Y. Yu, Modulating the electrolyte microenvironment in electrical double layer for boosting electrocatalytic nitrate reduction to ammonia, *Angew. Chem., Int. Ed.*, 2024, **63**, e202408382.

15 J. Guo, M. J. Liu, C. Laguna, D. M. Miller, K. S. Williams, B. D. Clark, C. Muñoz, S. J. Blair, A. C. Nielander, T. F. Jarillo and W. A. Tarpeh, Electrodialysis and nitrate reduction (EDNR) to enable distributed ammonia manufacturing from wastewaters, *Energy Environ. Sci.*, 2024, **17**, 8787–8800.

16 Y. Fan, Y. Yan, O. Nwokonkwo, D. J. Rivera, W. Pan, E. Chen, J.-Y. Kim, J. Simon, M. Saffer-Meng, X. Wang, C. Muhich and L. R. Winter, Tuning nitrate reduction reaction selectivity via selective adsorption in electrified membranes, *Nat. Chem. Eng.*, 2025, **2**, 379–390.

17 J. Sun, S. Garg and T. D. Waite, A novel integrated flow-electrode capacitive deionization and flow cathode system for nitrate removal and ammonia generation from simulated groundwater, *Environ. Sci. Technol.*, 2023, **57**, 14726–14736.

18 W. Zhong, X. Xiang, P. Chen, J. Su, Z. Gong, X. Liu, S. Zhao, N. Zhang, C. Feng, Z. Zhang, Y. Chen and Z. Lin, Shifting hydrogenation pathway via electronic activation for efficient nitrate electroreduction to ammonia in sewages, *Chem Catal.*, 2025, **5**, 101182.

19 S. Zhang, K. Li, X. Zhang, Y. Ye, T. Shi, Y. Jiang, L. Zheng, Y. Lin and H. Zhang, Concurrently Selective electrosynthesis of ammonia and glycolic acid over cathodic single-atom cobalt and anodic PdNi alloying catalysts, *Adv. Funct. Mater.*, 2024, **35**, 2415046.

20 B. Zhou, L. Yu, W. Zhang, X. Liu, H. Zhang, J. Cheng, Z. Chen, H. Zhang, M. Li, Y. Shi, F. Jia, Y. Huang, L. Zhang and Z. Ai, Cu₁–Fe dual sites for superior neutral ammonia electrosynthesis from nitrate, *Angew. Chem., Int. Ed.*, 2024, **63**, e202406046.

21 G. Zhang, X. Li, K. Chen, Y. Guo, D. Ma and K. Chu, Tandem electrocatalytic nitrate reduction to ammonia on MBenes, *Angew. Chem., Int. Ed.*, 2023, **62**, e202300054.

22 Y. Li, Z. Lu, L. Zheng, X. Yan, J. Xie, Z. Yu, S. Zhang, F. Jiang and H. Chen, The synergistic catalysis effect on electrochemical nitrate reduction at the dual-function active sites of the heterostructure, *Energy Environ. Sci.*, 2024, **17**, 4582–4593.

23 Z. Chang, G. Meng, Y. Chen, C. Chen, S. Han, P. Wu, L. Zhu, H. Tian, F. Kong, M. Wang, X. Cui and J. Shi, Dual-site W–O–CoP catalysts for active and selective nitrate conversion to ammonia in a broad concentration window, *Adv. Mater.*, 2023, **35**, 2304508.

24 J. Wei, J. Wang, W. Yu, J. Li, Y. Yang, Y. Wang, N. Li, R. Xu, L. Yang, G. Li and P. J. Dyson, Dual-active-site accelerated hydrogenation facilitates efficient electrochemical reduction of nitrate to ammonia, *Appl. Catal., B*, 2025, **378**, 125629.

25 W. Yang, Z. Chang, X. Yu, P. Wu, R. Shen, L. Wang, X. Cui and J. Shi, Cu–Co dual sites tandem synergistic effect boosting neutral low concentration nitrate electroreduction to ammonia, *Adv. Sci.*, 2025, **12**, 2416386.

26 X. Wang, L. Winter, X. Wu, Y. Fan, Y. Zhao, J. Kim and M. Elimelech, Intensified atomic utilization efficiency of single-atom catalysts for nitrate conversion via electrified nanoporous membrane, *Sci. Adv.*, 2025, **11**, eads6943.

27 M. Li, Y. Wen, Y. Fang and B. Shan, Molecular wiring of electrocatalytic nitrate reduction to ammonia and water oxidation by iron-coordinated macroporous conductive networks, *Angew. Chem., Int. Ed.*, 2024, **63**, e202405746.

28 T. Ren, Y. Sheng, M. Wang, K. Ren, L. Wang and Y. Xu, Recent advances of Cu-based materials for electrochemical nitrate reduction to ammonia, *Chin. J. Struct. Chem.*, 2022, **41**, 2212089.

29 H. Zhang, Z. Liu, H. Li, Z. Fu, G. Zhang, H. Zhang, G. Wang and Y. Zhang, PdFe alloy nanoparticles supported on nitrogen-doped carbon nanotubes for electrocatalytic upcycling of poly(ethylene terephthalate) plastics into formate coupled with hydrogen evolution, *J. Mater. Chem. A*, 2024, **12**, 15984–15995.

30 Y. Wang, W. Zhou, R. Jia, Y. Yu and B. Zhang, Unveiling the activity origin of a copper based electrocatalyst for selective



nitrate reduction to ammonia, *Angew. Chem., Int. Ed.*, 2022, **59**, 5350–5354.

31 H. Yin, J. Yuan, J. Wang, S. Hu, P. Wang and H. Xie, Crystalline nitrogen-doped-carbon anchored well-dispersed Fe_3O_4 nanoparticles for real-time scalable neutral H_2O_2 electrosynthesis, *Energy Environ. Sci.*, 2025, **18**, 2231–2242.

32 X. Yang, J. Prabowo, J. Chen, F. She, L. Lai, F. Liu, Z. Hua, Y. Wang, J. Fang, K. Goh, D. Zhang, H. Li, L. Wei and Y. Chen, Sonicated carbon nanotube catalysts for efficient point-of-use water treatment, *Adv. Mater.*, 2025, **37**, 2504618.

33 J. S. Li, H. Liu, F. Du, L. F. Liu, Y. J. Gu, C. M. Li, C. X. Guo and H. Y. Wang, Microenvironmental corrosion and hydrolysis induced two-dimensional heterojunction of copper oxide@ ferriferous oxide for efficient electrochemical nitrate reduction to ammonia, *Chem. Eng. J.*, 2023, **471**, 144488.

34 Z. Deng, C. Ma, Z. Li, Y. Luo, L. Zhang, S. Sun, Q. Liu, J. Du, Q. Lu, B. Zheng and X. Sun, High-efficiency electrochemical nitrate reduction to ammonia on a Co_3O_4 nanoarray catalyst with cobalt vacancies, *ACS Appl. Mater. Interfaces*, 2022, **14**, 46595–46602.

35 J. Liu, Y. Xiang, Y. Chen, H. Zhang, B. Ye, L. Ren, W. Tan, A. Kappler and J. Hou, Quantitative contribution of oxygen vacancy defects to arsenate immobilization on hematite, *Environ. Sci. Technol.*, 2023, **57**, 12453–12464.

36 T. S. Bui, Z. Ma, J. A. Yuwono, P. V. Kumar, G. E. P. O'Connell, L. Peng, Y. Yang, M. Lim, R. Daiyan, E. C. Lovell and R. Amal, *Adv. Funct. Mater.*, 2024, **34**, 2408704.

37 T. S. Bui, E. C. Lovell, R. Daiyan and R. Amal, Defective metal oxides: Lessons from CO_2 RR and applications in NO_x RR, *Adv. Mater.*, 2023, **35**, 2205814.

38 P. E. Larson, X-ray induced photoelectron and auger spectra of Cu, CuO , Cu_2O , and Cu_2S thin films, *J. Electron Spectrosc. Relat. Phenom.*, 1974, **4**, 213–218.

39 J. Ding, W. Li, H. Zhang, S. Tang, Z. Mao, S. Zhang, M. Jin, Q. Lin, Y. Zhang, G. Wang and H. Zhang, A cascade jet plasma oxidation-electroreduction system using Pd–Ni dual-site catalyst for sustainable ammonia production from air, *Adv. Funct. Mater.*, 2024, **34**, 2410768.

40 M. Chen, J. Bi, X. Huang, T. Wang, Z. Wang and H. Hao, Bi_2O_3 nanosheets arrays *in situ* decorated on carbon cloth for efficient electrochemical reduction of nitrate, *Chemosphere*, 2021, **278**, 130386.

41 V. K. Agrawal and M. Trenary, *Surf. Sci.*, 1991, **259**, 116.

42 M. C. Figueiredo, J. Souza-Garcia, V. Climent and J. M. Feliu, Nitrate reduction on $\text{Pt}(1\ 1\ 1)$ surfaces modified by Bi adatoms, *Electrochem. Commun.*, 2009, **11**, 1760.

43 G. Zhang, X. Li, K. Chen, Y. Guo, D. Ma and K. Chu, Tandem electrocatalytic nitrate reduction to ammonia on MBenes, *Angew. Chem., Int. Ed.*, 2023, **62**, e2300054.

44 V. Rosca, G. L. Beltramo and M. T. M. Koper, Hydroxylamine electrochemistry at polycrystalline platinum in acidic media: a voltammetric, DEMS and FTIR study, *J. Electroanal. Chem.*, 2004, **566**, 53.

45 Z. Song, Y. Liu, Y. Zhong, Q. Guo, J. Zeng and Z. Geng, Efficient electroreduction of nitrate into ammonia at ultra-low concentrations via an enrichment effect, *Adv. Mater.*, 2022, **34**, 2204306.

46 Z. Chen, Y. Zhao, H. Huang, G. Liu, H. Zhang, Y. Yan, H. Li, L. Liu, M. Liu, D. Wang and J. Zeng, Isolated copper atoms boost $^*\text{NO}_3$ adsorption and active hydrogen retention over zinc oxide for ammonia electrosynthesis at ampere-level current densities, *J. Am. Chem. Soc.*, 2025, **147**, 18737–18746.

47 H. Guo, Y. Zhou, K. Chu, X. Cao, J. Qin, N. Zhang, M. B. J. Roeffaers, R. Zbořil, J. Hofkens, K. Müllen, F. Lai and T. Liu, Improved ammonia synthesis and energy output from zinc-nitrate batteries by spin-state regulation in perovskite oxides, *J. Am. Chem. Soc.*, 2025, **147**, 3119–3128.

